JGR Oceans

RESEARCH ARTICLE
10.1029/2023JC020006

Sea Ice-Driven Variability in the Pacific Subantarctic Mode Water Formation Regions

R. N. C. Sanders[1,2,3], A. J. S. Meijers[1], P. R. Holland[1], and A. C. Naveira Garabato[2]

[1]British Antarctic Survey, Cambridge, UK, [2]University of Southampton, Southampton, UK, [3]Now at NORCE Norwegian Research Centre, Bjerknes Centre for Climate Research, Bergen, Norway

Key Points:

- Temperature and salinity variability at Pacific Subantarctic Mode Water (SAMW) formation sites is driven by surface fluxes, advection and entrainment
- Freshwater anomalies advected from the Ross Sea take up to 2 years to reach the Pacific SAMW formation regions
- Anomalies in Amundsen/Bellingshausen sea ice in 2016–2017 drove salinity anomalies at the nearby southeast Pacific SAMW formation site

Correspondence to:

R. N. C. Sanders,
rasa@norceresearch.no

Citation:

Sanders, R. N. C., Meijers, A. J. S., Holland, P. R., & Naveira Garabato, A. C. (2023). Sea ice-driven variability in the Pacific subantarctic mode water formation regions. *Journal of Geophysical Research: Oceans*, *128*, e2023JC020006. https://doi.org/10.1029/2023JC020006

Received 5 MAY 2023
Accepted 31 OCT 2023

Abstract Subantarctic Mode Water (SAMW) forms north of the Subantarctic Front, in regions of deep winter mixed layers, and is important to the absorption and storage of anthropogenic CO_2 and heat. Two SAMW pools exist in the Pacific, a lighter Central mode (CPSAMW), and a denser Southeast mode (SEPSAMW). Both have experienced significant interannual variability in thickness and properties in recent years. We compute mixed layer temperature and salinity budgets for the two SAMW formation regions, to determine the relative contribution of processes driving variability in the properties of mixed layers that subduct to form SAMW. The dominant drivers of temperature and salinity variability are shown to be surface fluxes, horizontal advection, and entrainment of deeper water. Salt advection into each SAMW formation region is found to be strongly correlated with changes in sea ice area in the northern Ross Sea, with lags of up to 2 years. Further correlation is found between meridional salt advection in the southeast Pacific formation regions, and sea ice area in the northern Amundsen/Bellingshausen seas, suggesting that freshwater derived from sea ice melt reaches the SEPSAMW formation region within 6 months. In 2016, strong advective freshening of the SEPSAMW formation region, linked to increased winter sea ice in the Amundsen/Bellingshausen seas, led to anomalously fresh mixed layers. However, a regime change in Antarctic sea ice in 2016 resulted in a subsequent lack of the usual advective freshening in the SEPSAMW formation region, driving increased salinity of the mixed layer the following year.

Plain Language Summary Well-mixed mode waters that form in the north of the Southern Ocean are particularly important to the ocean absorption of heat and CO_2 from the atmosphere. Two types of mode water form in the Pacific sector of the Southern Ocean: a Central pool and a Southeast pool. Both have shown significant year-to-year variability in recent decades. Variability in the regions where these waters form is shown to be due to changes in air-sea fluxes, horizontal advection, and the upward transport of deeper water. Transport of freshwater into the mode water formation regions is shown to be correlated with year-to-year changes in sea ice area in the Ross Sea and in the Amundsen/Bellingshausen seas. The results suggest that it takes around 6 months for sea ice melt from the Amundsen/Bellingshausen seas to reach the southeast mode water region, and up to 2 years for freshwater from the Ross Sea to reach both mode water formation sites. In 2015, Amundsen/Bellingshausen sea ice was particularly high, leading to more freshwater being transported to the southeast mode water site the following spring/summer. A huge decrease in winter sea ice in 2016 then caused the opposite, and salinity at the formation site was unusually high.

1. Introduction

Subantarctic Mode Water (SAMW) forms in the Southern Ocean, north of the Subantarctic Front (SAF), in regions of deep winter mixed layers (McCartney, 1977). The deep mixed layers are generated by a number of processes, including wind-driven mixing, surface heat loss, Ekman transport, and eddy diffusion (Holte et al., 2012; Qu et al., 2020; Sallée et al., 2008). Subduction of SAMW occurs in winter when the mixed layers are deepest, and water is transferred directly from the mixed layer to the permanent thermocline. During the following spring/summer, the water column stratifies and the SAMW is trapped beneath the shallow seasonal mixed layer. Two SAMW pools with different properties exist in the Pacific sector: a lighter central pool (CPSAMW) and a denser Southeast pool (SEPSAMW) (Cerovečki et al., 2019). The formation regions of the two pools are separated by the Pacific Antarctic Ridge at approximately 115°W, and each pool has been shown to experience significant interannual variability in depth and properties, often out of phase with one another (Cerovečki & Meijers, 2021; Meijers et al., 2019). Once subducted, SAMW flows equatorward into the subtropical ocean basins. Formation of the water mass has particular importance to the ocean uptake of anthropogenic heat and CO_2 (Ito et al., 2010;

Sabine et al., 2004). An increase in heat uptake by the Southern Ocean in recent years has been connected to an increase in thickness and volume of SAMW (Gao et al., 2018; Jing & Luo, 2021).

SAMW variability has different drivers in each ocean basin (Downes et al., 2017), with Pacific SAMW thickness strongly correlated with buoyancy fluxes (Wang et al., 2022). Particularly strong anomalies in the properties of Pacific SAMW were observed in 2016, with deep winter mixed layers in the central Pacific formation region, and shallow winter mixed layers in the southeast Pacific (Meijers et al., 2019). The shallow mixed layers in the southeast have been linked to a lack of winter storms, causing reduced heat loss to the atmosphere (Ogle et al., 2018; Tamsitt et al., 2020).

A weak net increase in Antarctic sea ice cover, associated with wind-driven changes in sea ice transport, was observed from the late 1970s (Comiso & Nishio, 2008; Holland & Kwok, 2012), with the largest increase in the Ross Sea (Parkinson & Cavalieri, 2012). The trend ceased in 2016, when a rapid decrease occurred and sea ice extent dropped to a record minimum (Schlosser et al., 2018). Increased sea ice leads to increased seasonal melting at the ice edge, with freshwater added to the upper Southern Ocean overturning cell (Abernathey et al., 2016; Holland & Kwok, 2012), where it can influence SAMW formation. This is particularly the case in the Pacific sector, where the primary SAMW formation regions are significantly closer to regions of sea ice melt compared to the Indian Ocean sector. An increase in northward freshwater transport via sea ice was observed from 1982 to 2008, with the strongest trend in the Pacific sector (Haumann et al., 2016). Outcropping isopycnals within the Antarctic Circumpolar Current (ACC) region are close together, so small changes in the spatial distribution of sea ice melt have the potential to cause significant variability in the properties of the water masses formed in the region (Cerovečki et al., 2019). Sea ice variability has been suggested to play a role in setting SAMW properties; particle release experiments indicate that freshwater derived from sea ice melt in the Ross Sea can reach the SEPSAMW formation region within 2 years (Cerovečki et al., 2019).

Here, we examine the processes and pathways by which variability in sea ice melt and extent may impact SAMW formation and properties. We focus on the Pacific Ocean due to the proximity between sea ice and water mass formation sites. We compute mixed layer temperature and salinity budgets for the SAMW formation regions, using the output of two ocean state estimates: ECCO version 4 (ECCO), and the biogeochemical Southern Ocean state estimate (B-SOSE). We use budget calculations to determine the processes connecting anomalies in Antarctic sea ice area to anomalies in the properties of the SAMW formation regions. We use the 24-year-long ECCO record to understand the processes driving variability in the mixed layers of the SAMW formation regions, and the shorter, higher-resolution B-SOSE time series to focus on the causes of the strong anomalies observed in the SAMW formation regions during the winter of 2016.

2. Methods

2.1. ECCO

ECCO is a MITgcm-based global ocean state estimate; the initial conditions, mixing parameters and surface forcing are iteratively adjusted, via the adjoint method, to reduce the differences between the modeled ocean state and available observations (Forget, Campin, et al., 2015). The state estimate provides a physically consistent, property-conserving description of the ocean, driven by observed boundary conditions, so can be used to identify the processes behind observed ocean variability. ECCO is initially forced by ERA-Interim atmospheric fields. ECCO version 4, release three covers the period January 1992–December 2015, with a nominal spatial resolution of 1°, and 50 vertical levels with varying thickness of 10–456 m. We use the monthly averaged output of the state estimate. ECCO has been used in many previous studies, both globally and in the Southern Ocean, and has been shown to be consistent with available observations (Boland et al., 2021; ECCO Consortium, 2017a, 2017b; Forget, Campin, et al., 2015; Fukumori et al., 2017). While a range of observational data sets covering different time periods are used to constrain sea ice in ECCO, leading to variations from any particular set of observations, mean September sea ice in ECCO has been validated against satellite data previously by Su (2017). Sea ice area in the regions focused on in this study was compared against the same satellite data (Meier et al., 2021), and shown to have very similar seasonal and interannual variability with an r^2 value of at least 0.7 for each model (Figure S1, https://nsidc.org/data/g02202/versions/4).

2.2. B-SOSE

B-SOSE is another MITgcm-based state estimate, but covers only the Southern Ocean south of 30°S, with a spatial resolution of $\frac{1}{6}$° and 52 vertical levels with varying thickness of 4.2–400 m (Verdy & Mazloff, 2017).

We use the 3-day averaged output of iteration 122, which covers a 6 year period from 2013 to 2018. As a state estimate, B-SOSE is also constrained by available observations and, like ECCO, is initially forced by ERA–Interim atmospheric data. The various iterations of B-SOSE have been used in a number of studies (e.g., Russell et al. (2018); Beadling et al. (2020); Thomas et al. (2021)). Jersild and Ito (2020) showed B-SOSE winter mixed layer depths and surface temperatures to be consistent with observations. Both models also show very similar seasonal variability in potential vorticity in the Pacific sector of the Southern Ocean, indicating that the seasonal cycle in SAMW formation matches observations (Figure S2, https://doi.org/10.5285/961f3c2d-04ca-1911-e053-6c86abc0150b). While sea ice area is slightly overestimated in B-SOSE in comparison to satellite observations (Figure S1, https://nsidc.org/data/g02202/versions/4), the observed interannual variability is reproduced well by the model.

2.3. Defining SAMW Formation Regions

Four spatial boxes are used to define the regions of interest to this study (Figure 1): two northern boxes for the SAMW formation regions, previously used by Meijers et al. (2019), and two boxes directly south of these. The southern boxes are defined to better understand export pathways from the sea ice edge to the SAMW formation regions. The CPSAMW box is defined as 160–114°W, 47.3–55.3°S, and the SEPSAMW box as 114–74°W, 47–59°S. A distinct mixed-layer depth (MLD) maximum is seen in each SAMW box, with a shoaling between, at the approximate location of the Pacific Antarctic Ridge, matching observations. MLD is defined as the depth at which density is 0.03 kg m^{-3} greater than at the surface—an estimate shown to be a good representation of Southern Ocean MLDs (de Boyer Montégut et al., 2004). To capture only the area where deep winter convection occurs, the SAMW formation sites are defined as the area within the boxes with a maximum MLD of at least 350 m.

The two boxes directly south of the SAMW boxes are defined approximately between the SAF and the Polar Front, bordered by the most southerly position of the Polar Front. These boxes are used to more easily track the transport of freshwater anomalies from the sea ice zone to the SAMW formation sites. We describe them as the central Pacific Polar Front (CPPF) box, defined as 160–114°W, 55.3–62.°S and the southeast Pacific Polar Front (SEPPF) box, defined as 114–72°W, 59–63.8°S.

2.4. Mixed Layer Budgets

SAMW ultimately forms from the subducted mixed layer waters within the formation regions, so computing mixed layer budgets at these sites allows the processes setting the properties of subducted SAMW to be ascertained. We therefore compute temperature and salinity budgets in these regions using both state estimates. While it is possible to compute fully closed budgets from the model output advective and diffusive terms, these budgets are computed for individual model cells, and while the budgets in these individual depth cells can be averaged over the mixed layer at a particular longitude-latitude point, the result will not take into account the temporal and spatial variability in MLD. This variability is particularly important within the SAMW formation due to the seasonal deepening of the deep winter mixed layers, which can drive temperature and salinity change via entrainment and lateral induction (Huang, 1990).

We instead use a set of equations to compute a kinematic approximation of the mixed layer budgets within the SAMW formation regions. This method takes into account the spatio-temporal variability in MLD, and therefore includes the concepts of entrainment and lateral induction, providing insights into the evolution of the mixed layer and its impact on temperature and salinity. We start by integrating the model output temperature, salinity and horizontal velocity over a mixed layer of depth h_m, and use them to calculate each budget term in Equations 1 and 2, following the methods used in a number of previous studies (Close & Goosse, 2013; Dong et al., 2007, 2009; Peter et al., 2006; Ren et al., 2011; Sanders et al., 2022).

$$\frac{\partial S_m}{\partial t} = \frac{Q_{fw} S_m}{\rho_0 h_m} - \mathbf{u_m} \cdot \nabla S_m - \frac{\partial h_m}{\partial t}\frac{\Delta S}{h_m} - \mathbf{u_m} \cdot \nabla h_m \frac{\Delta S}{h_m} + \frac{K_z}{h_m}\frac{\partial S}{\partial z} + \kappa \nabla^2 S_m \tag{1}$$

$$\frac{\partial T_m}{\partial t} = \underbrace{\frac{Q_h - q(h_m)}{\rho_0 c_p h_m}}_{\text{Surface flux}} \underbrace{- \mathbf{u_m} \cdot \nabla T_m}_{\text{Advection}} \underbrace{- \frac{\partial h_m}{\partial t}\frac{\Delta T}{h_m}}_{\text{Entrainment}} \underbrace{- \mathbf{u_m} \cdot \nabla h_m \frac{\Delta T}{h_m}}_{\text{Lateral induction}} + \underbrace{\frac{K_z}{h_m}\frac{\partial T}{\partial z}}_{\text{Vertical diffusion}} + \underbrace{\kappa \nabla^2 T_m}_{\text{Horizontal diffusion}} \tag{2}$$

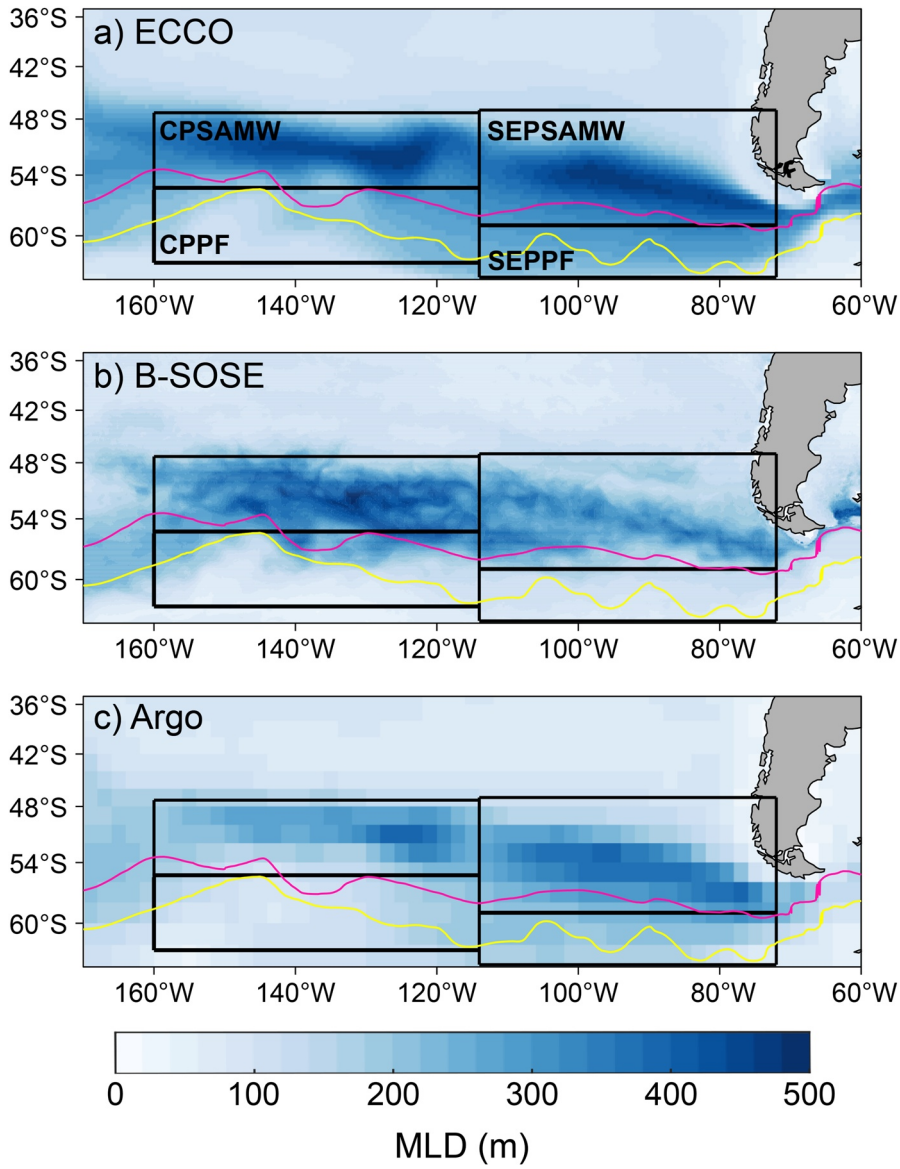

Figure 1. Average winter mixed-layer depth (m) in the Pacific sector of the Southern Ocean in (a) ECCO, (b) B-SOSE, and (c) Argo observations. The boxes show the four regions of interest: two SAMW formation regions and two regions directly south, within the Polar Front. The positions of the Polar Front (yellow) and Subantarctic Front (pink), defined by Boehme et al. (2008), are also shown.

Each term on the right hand side gives the change in the average salinity/temperature of the mixed layer (S_m, T_m), due to each potential process: surface fluxes, horizontal advection, entrainment of deeper water, lateral induction, and vertical and horizontal diffusion. Q_{fw} and Q_h are the model output net surface freshwater and heat flux fields (positive downwards); the freshwater flux includes a sea ice component where relevant. ρ_0 and c_p denote the seawater reference density and specific heat capacity, and the function q represents the decay of shortwave radiation within the top model depth cells. $\boldsymbol{u}_m$ is the average mixed layer lateral ocean velocity, and ΔS and ΔT are the salinity/temperature difference between the mixed layer and the depth cell immediately below. Entrainment velocity is defined as the rate of change in h_m, set to zero when the mixed layer is shallowing, as detrainment does not alter the properties of the remaining water in the mixed layer. K_z and κ represent the vertical and horizontal diffusivity at the base of the mixed layer; these values are not comparable with the background mixing in the models, as there are multiple mixing schemes present in the models that represent diffusion. The diffusivity values at the mixed layer base are highly uncertain, so we simply choose constant values that are optimal for closing the budget within this specific

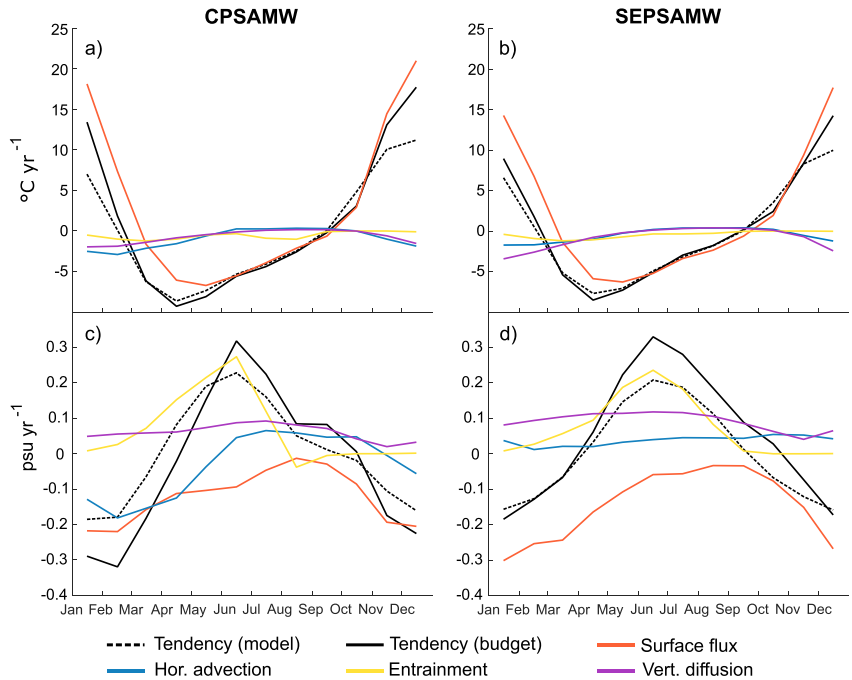

Figure 2. (a), (b) The average seasonal cycle of the ECCO mixed layer (a), (b) temperature budget (°C yr^{-1}) and (c), (d) salinity budget (psu yr^{-1}) averaged over the CPSAMW (left) and SEPSAMW (right) formation regions. The dashed black line is the rate of change in model output temperature/salinity and the solid black line is the sum of the budget terms. The remaining lines are the processes driving the temperature/salinity change.

region, that is, the values that most reduce the mismatch between the left and right hand sides of both equations, with different values selected north and south of the SAF. K_z was therefore chosen as 5.5×10^{-5} m^2 s^{-1} north of the SAF and 3.6×10^{-4} m^2 s^{-1} south of the SAF, and κ as 150 m^2 s^{-1} north of the SAF, and 800 m^2 s^{-1} south of the SAF.

This approach to computing budgets also has the advantage that it can be used across a range of model and observational data sets, including models where all budget diagnostics are not available. However, due to the coarse resolution of the model output, and the assumptions made to simplify the equations, such as the constant values for diffusivity and definition of entrainment velocity, there is still some lack of closure in the budgets, with a residual between the model output salinity/temperature tendency and the sum of the individual budget terms.

3. Results

3.1. Drivers of Variability in the Pacific SAMW Formation Regions

The average (1992–2015) seasonal cycles of the ECCO mixed layer temperature and salinity budgets, spatially averaged over the two Pacific SAMW formation regions, are shown in Figure 2. The full time-varying budgets for the 2013–2018 B-SOSE time series are shown in Figure 3, as the time series is too short to produce a meaningful average seasonal cycle. The same processes are responsible for driving the majority of temperature and salinity changes in both models, but the magnitude of the terms is higher in B-SOSE. In both models, the impact of lateral induction and horizontal diffusion in the SAMW formation regions is negligible in comparison to the dominant terms of the temperature and salinity budgets. The temperature budgets are dominated by surface heating, with very similar seasonal cycles in both regions (Figures 2a and 2b and 3a and 3b). Surface fluxes drive a maximum cooling in April/May in both SAMW formation regions, and a maximum warming in December/January. In B-SOSE, the maximum surface warming in January 2017 in the CPSAMW formation region, and in January 2016 in the SEPSAMW formation region. The surface flux term of the mixed layer budget is dependent on both the heat/freshwater flux into the surface ocean, and MLD, so stronger warming/freshening is indicative of a higher surface flux and/or a shallower mixed layer, as the fluxes are acting upon a smaller volume of water.

Horizontal advection, vertical diffusion, and entrainment play lesser roles, acting predominantly to cool the mixed layer. The strongest advective cooling in ECCO occurs in February and the strongest cooling via vertical

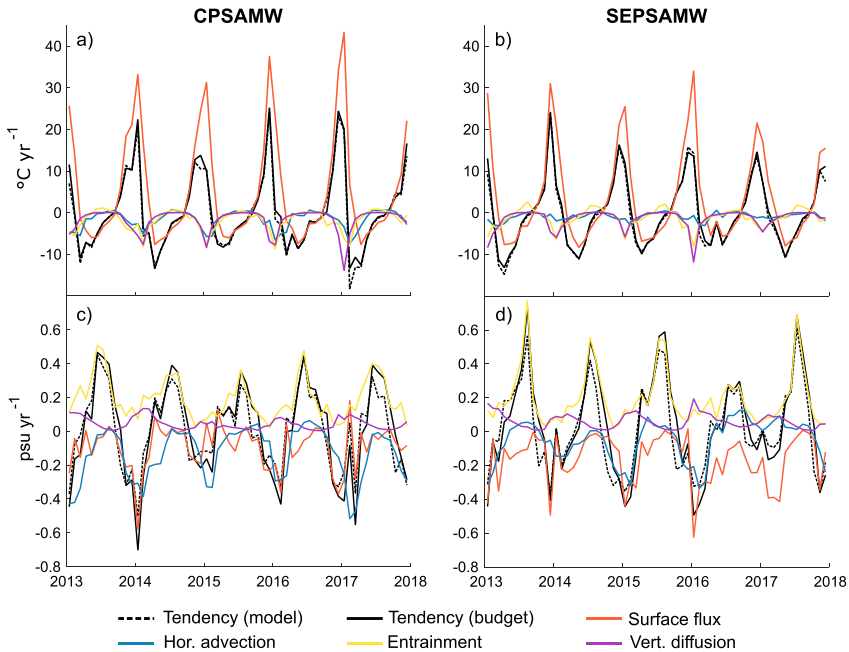

Figure 3. The B-SOSE 2013–2018 mixed layer (a), (b) temperature budget (°C yr^{-1}) and (c), (d) salinity budget (psu yr^{-1}), averaged over the CPSAMW (left) and SEPSAMW (right) formation regions. The dashed black line is the rate of change in model output temperature/salinity and the solid black line is the sum of the budget terms. The remaining lines are the processes driving the temperature/salinity change.

diffusion in January. In B-SOSE, the maximum diffusive cooling occurs in January 2017 in the CPSAMW formation region, and in January 2016 in the SEPSAMW formation region. Advection in B-SOSE drives a similar level of cooling each January–February, except during 2017, when advection instead drives a slight warming of the SEPSAMW formation region, suggesting either a reversal of the current or of the temperature gradient. There are two seasonal peaks in cooling via entrainment, one in March and a second from July–August, however the effect on mixed layer temperature is limited, with the maximum cooling never exceeding −1.2°C yr^{-1} in ECCO. Entrainment drives a cooling from around December to March in B-SOSE, reaching a maximum during January 2016 in each region, and drives a negligible change in temperature during the winter.

The salinity budgets between the two SAMW formation regions are more varied (Figures 2c and 2d and 3c and 3d), but in both the dominant drivers are entrainment, surface fluxes and horizontal advection. Surface freshwater fluxes drive a salinity decrease throughout the year, peaking in ECCO during austral summer, with the strongest surface freshening in B-SOSE occurring in January 2014 in the CPSAMW formation region, and January 2016 in the SEPSAMW formation region. As with the surface heat flux term, the salinity change due to surface fluxes is affected by both the net surface flux and MLD. Entrainment predominantly increases the salinity of the mixed layer as the mixed layer deepens and entrains higher-salinity water from below, reaching a maximum during June in ECCO. In B-SOSE, the peak in entrainment is generally a month later, reaching a maximum in the winter of 2013. Entrainment is particularly low in the winter of 2016 in the SEPSAMW formation region, reaching only 0.28 psu yr^{-1}, indicating either a reduction in the deepening of the winter mixed layer, or in the salinity gradient across the base of the mixed layer. The winter mixed layer in the SEPSAMW formation region during 2016 was observed to be anomalously shallow (Ogle et al., 2018), explaining the lower salt entrainment.

The role of salt advection in ECCO is very different in the two regions, playing a smaller role in the SEPSAMW formation region, but driving an overall slight salinity increase. In the CPSAMW formation region, advection instead freshens the mixed layer in spring/summer, and increases salinity in autumn/winter. In the later years covered by B-SOSE, advection generally drives a strong freshening in austral summer, with a peak of −0.52 psu yr^{-1} in the CPSAMW formation region in February 2017 and of −0.33 psu yr^{-1} in the SEPSAMW formation region in February 2016. The following summer of 2016/2017, advection does not drive the regular freshening, and is instead close to zero. During this period, the advection-driven cooling is also much smaller than usual, reaching only −1.3°C yr^{-1}, compared to a maximum of −3.1°C yr^{-1}.

In both models, the non-closure in the budget (the difference between the two black lines in Figures 2 and 3) is higher in the salinity budget than the temperature budget. This is likely because surface fluxes, which are derived directly from the models and so contain no budget calculation error, dominate the temperature budget. Despite the lack of closure in the budgets, the variability is similar between the two tendency calculations. Both models show a similar seasonality in the error, with the salinity budget tendency too negative from approximately November to May and too positive from May to November. This may be a result of the choice of constant diffusivity in the budgets. In the following sections, we focus on the advection and surface flux terms of the budgets, which are known to be accurate for the models, as they are computed in the same way using this method in the closed budget representation computed by model output terms.

3.2. Salt Advection in the Pacific SAMW Formation Regions in ECCO

Surface fluxes, advection and entrainment all play important roles in driving salinity variability in the SAMW formation regions. While entrainment dominates in winter, it is surface fluxes and horizontal advection that largely drive salinity changes in the lead up to wintertime SAMW subduction (approximately November–March), and therefore play a role in preconditioning subsequent winter convection. In this section, we examine how advection of freshwater into the formation sites varies on interannual timescales and drives changes in mixed layer properties in ECCO. While the advection term of the budgets is fairly small on annual timescales, once the average seasonal cycle has been removed, advection drives significant anomalies in the overall rate of change in salinity within the mixed layer, and can dominate in individual freshening events (Figure 4, left panels). This is true for salt advection in both the zonal and meridional directions (Figure 4, right panels).

In the CPSAMW formation region, salt advection anomalies are often in phase with the overall salinity tendency, and are of a similar magnitude (Figure 4a), suggesting an important role for advection in setting interannual variability. The strongest advection anomalies of 0.08 psu yr^{-1} occur from 2008–09, coinciding with the most strongly negative tendency anomalies of 0.09 psu yr^{-1}. Both zonal and meridional anomalies are important to the variability in advection in the region (Figure 4b). Advection does not play as strong a role in the SEPSAMW formation region, but is important in specific years, driving positive anomalies of 0.05 psu yr^{-1} due to zonal advection in 2006 and negative anomalies of −0.05 psu yr^{-1} in 2009–10 (Figure 4c), due to both zonal and meridional advection (Figure 4d).

Anomalies in salt advection and tendency are larger and more strongly correlated in the Polar Front regions. In the CPPF box, salt advection anomalies are again of a similar magnitude to those in the overall salinity tendency, and the two are generally in phase, with a correlation coefficient of 0.62 (Figure 4e). Particularly strong freshening occurs from 2007 to 2008, around a year earlier than the strong advective freshening in the CPSAMW formation region. The most negative advection anomalies occur in April 2009, reaching −0.15 psu yr^{-1}, compared to total tendency anomalies of −0.13 psu yr^{-1}. Meridional advection anomalies are larger than those in zonal advection from 1995 to 2004, but the peak in 2008 is a result of strong zonal anomalies of −0.16 psu yr^{-1} (Figure 4f). The SEPPF box experiences particularly strong salt advection, similar to the overall tendency, with a correlation coefficient of 0.77 (Figure 4g). Salt advection anomalies range from −0.17–0.11 psu yr^{-1}, with the strongest advective freshening in the summer of 2009/10, driven by strong anomalies in meridional advection. Over the time series, both zonal and meridional advection anomalies are larger than in any other water mass formation region, with zonal anomalies of −0.10–0.10 psu yr^{-1}, and meridional anomalies of −0.16–0.08 psu yr^{-1} (Figure 4h).

Salt advection is generally lowest in the SEPSAMW formation region, but still drives significant interannual variability. In the other water mass formation regions, advection drives anomalies in the rate of change in salinity that are of a similar, and frequently greater, magnitude than those in the total salinity tendency. In particular, tendency anomalies in the Polar Front boxes are very strongly correlated to the advective fluxes. These boxes are significantly closer to the regions of sea ice melt than the SAMW boxes, and the importance of the advective signal within them suggests that sea ice melt may be an important contributor to the advective signals. In each region, zonal and meridional advection both provide important contributions to the overall salt advection anomalies. In the SEPPF box, zonal and meridional contributions are comparable, with similar frequencies, although they are often out of phase. This area is likely to be influenced by zonal advection of freshwater anomalies from the Ross Sea, and meridional advection of freshwater anomalies from the Amundsen/Bellingshausen seas immediately south. In the other regions, zonal and meridional advection anomalies have different frequency structures, suggesting different sources (Figure 4).

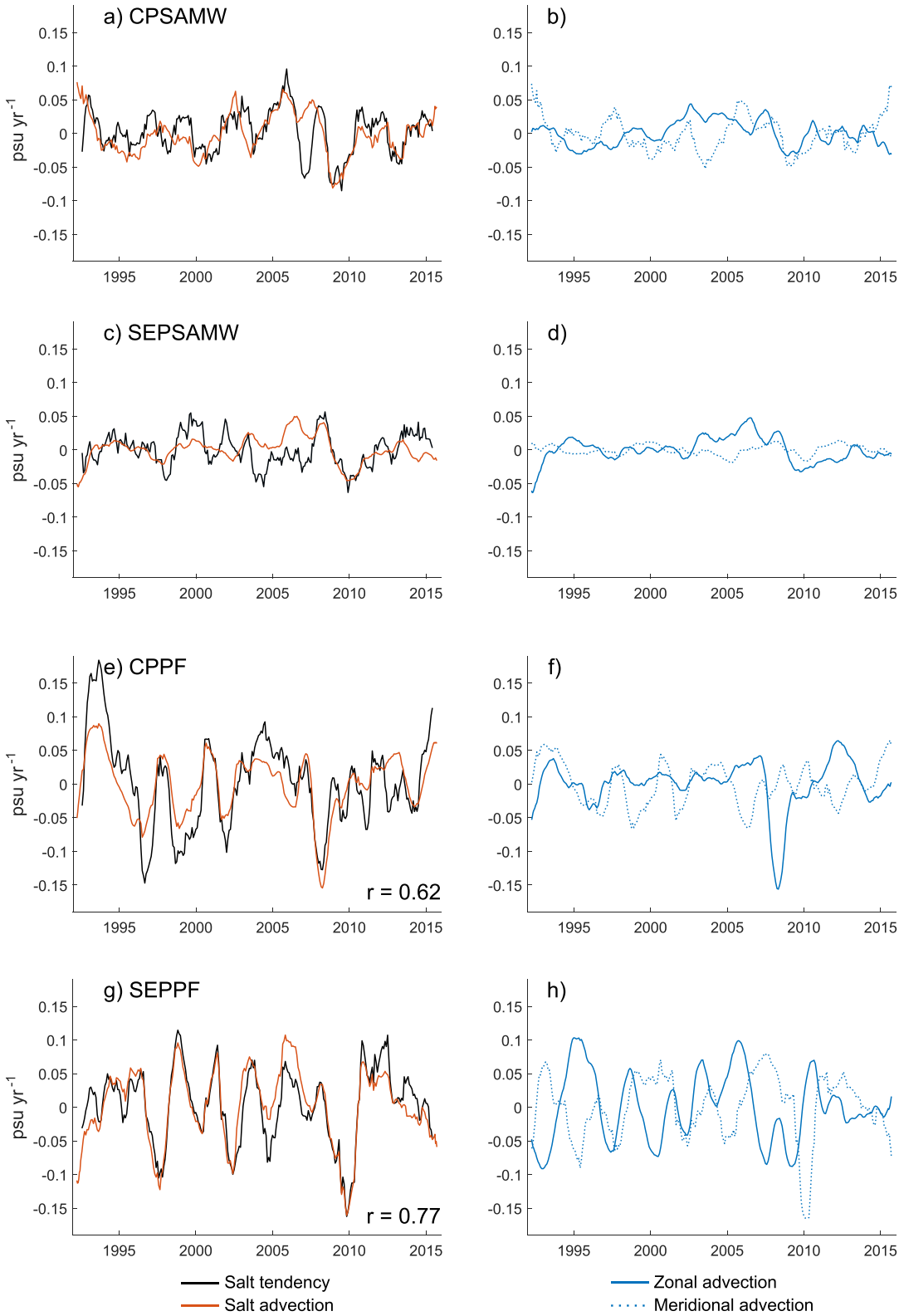

Figure 4. Detrended anomalies in ECCO mixed layer salt tendency and advection (left), and the zonal and meridional components of the advection (right), averaged over each water mass formation region, with a 12-month moving average applied (psu yr^{-1}). When significant ($p < 0.01$), the correlation coefficient, r, is shown.

3.3. Connection Between ECCO Sea Ice and Salinity Budget Anomalies

The higher significance of the advective component to the overall salt budget in the more southerly Polar Front boxes is suggestive of a role for sea ice melt in contributing to interannual variability in these water mass formation regions. Significant negative correlations are found between annual averaged sea ice area and salt advection in each water mass formation region across much of the Ross, Amundsen and Bellingshausen seas (Figure 5). Annual averaged ECCO sea ice is computed for January–December of each year, and correlated with the annual averaged advection from January to December for zero lag, February–January for a 1 month lag, and so on.

The strongest negative correlation is found for sea ice north of around 66°S, as there is less sea ice variability closer to the Antarctic coast. Correlation is significantly negative between advection in each water mass formation region and sea ice area in the northern Ross Sea, and the lag of the strongest correlation increases with increasing distance to the water mass formation site. The approximately 2 year lag in the SAMW formation regions is similar to that seen in a particle release experiment by Cerovečki et al. (2019), suggesting that advection of sea ice meltwater causes the correlation. In the Amundsen/Bellingshausen seas, directly south of the Southeast water mass formation regions, there are patches of significant negative correlation between sea ice area and salt advection in only the southeast water mass formation regions (Figures 5c and 5g), with a lag that increases with distance from the sea ice edge (Figures 5d and 5h), suggesting the correlation is related to sea ice. The lag of this correlation is lower than that in the Ross Sea, due to the proximity of the boxes to the sea ice edge. The lack of correlation between the Amundsen/Bellingshausen seas and the CPSAMW and CPPF gives confidence that a causal link is being captured by these correlations, as there is no advective pathway between these regions due to the eastward-flowing ACC.

The Ross Sea box in Figure 5 covers the sea ice area that has strong correlation, between −0.5 and −0.7 ($p < 0.05$), with salt advection in all four regions: 175°E−145°W. The Amundsen/Bellingshausen seas box covers the sea ice area where correlation is strong, between −0.74 and −0.84 ($p < 0.05$), with advection in only the SEPSAMW and SEPPF formation regions (as this region is downstream of the central Pacific regions): 74–114°W. While there are other regions of strong correlation, such as between the two boxes, the very low lag suggests that other processes are indirectly driving the correlation.

The correlation was also tested between sea ice and the other ECCO mixed layer budget terms. No significant correlation was found with any temperature budget term (not shown), likely because temperature is strongly influenced by surface fluxes away from the sea ice zone, which will erode any surface anomalies due to sea ice melt as they are advected north. While significant correlation is observed between sea ice area and total salinity tendency in both SAMW formation regions, it is weaker than that with only advection, due to the contribution of other, more local, processes, such as surface fluxes and entrainment. The correlation was also tested between salt advection and sea ice volume but was found to be slightly weaker than with sea ice area, suggesting that the surface area covered by sea ice, and particularly its northward extent and distance from the SAMW formation regions, is important, as well as the amount of freshwater deposited into the surface at the sea ice edge.

During the ECCO time series (1992–2015), there is significant interannual variability in sea ice area within the two sea ice boxes (Figure 6). Detrended anomalies in sea ice area are particularly high in the Ross Sea box in the winters of 1998/99 and 2007/08, with a notable minimum around 2005, while the highest Amundsen/Bellingshausen seas sea ice area is in 2009/10 (Figure 6). Subsequent variability in the freshwater flux into the surface ocean, calculated from the model freshwater flux output fields, is strongly correlated with sea ice area, with a correlation coefficient of 0.76 in the Ross Sea and 0.69 in the Amundsen/Bellingshausen seas.

3.4. Link Between Ross Sea Sea Ice and Salt Advection in ECCO

Significant ($p < 0.05$) negative correlation is shown between ECCO sea ice area in the northern Ross Sea and salt advection in the CPPF region for lags of 0–12 months, peaking at 3 months with a correlation coefficient of −0.70 (Figure 7a), indicating freshening associated with increased sea ice area and subsequent melt. This short lag time is expected as the CPPF box overlaps with the sea ice area (see inset map of Figure 7a). The SEPPF box then experiences significant correlation at a 13–21 months lag, with the strongest correlation of −0.50 at 14 months, suggesting that it takes just over one year for freshwater anomalies to advect eastward across the Pacific sector from the Ross Sea. Significant correlation occurs in the CPSAMW formation region at a 14–23 months lag, peaking at −0.61 at 16 months, and significant correlation of up to −0.57 occurs in the SEPSAMW formation region at a 17–35 months lag, peaking at 28 months. This suggests that freshwater anomalies take around 2 years

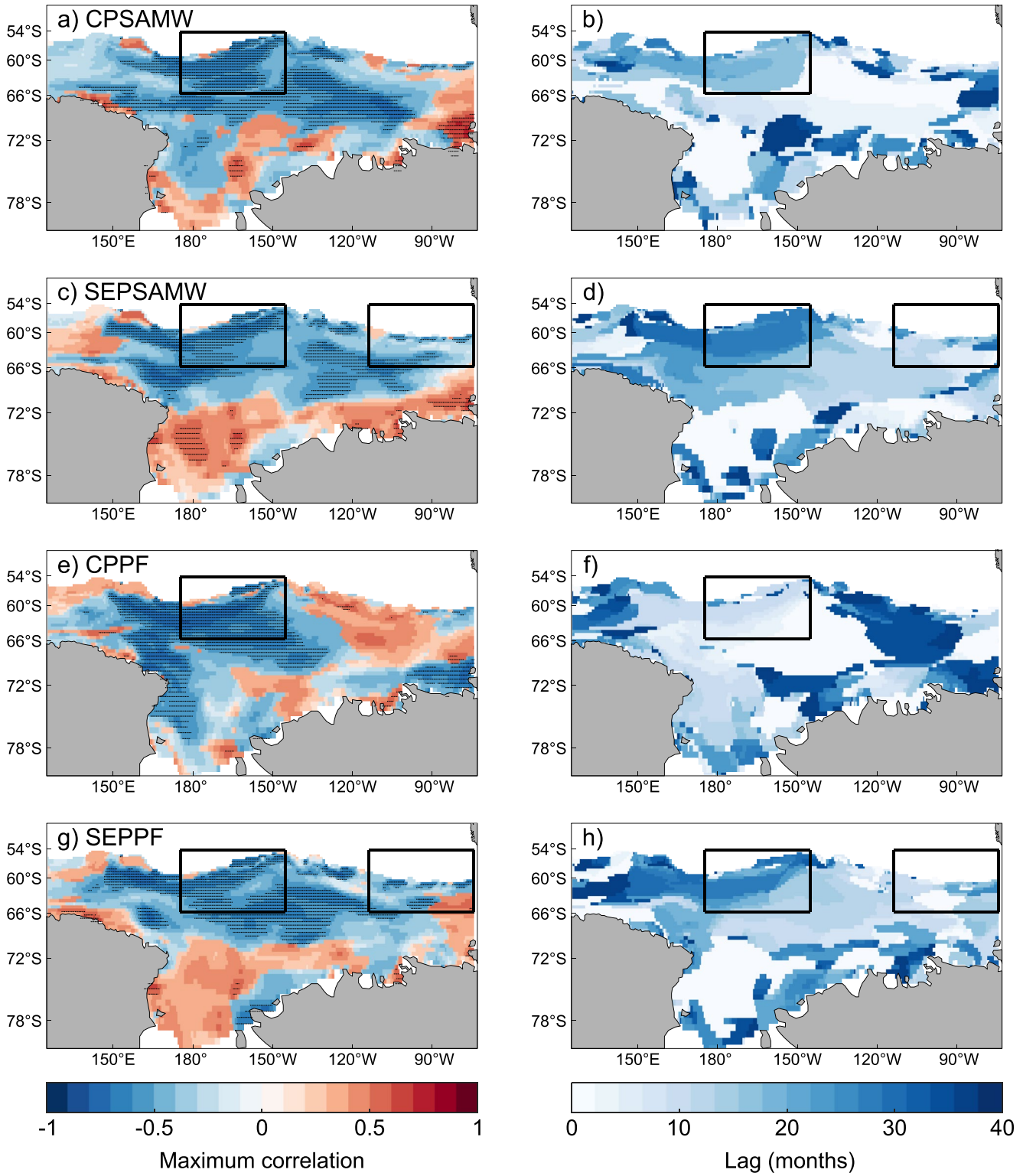

Figure 5. Maximum correlation coefficient (left) between the ECCO annual averaged sea ice area at each point and salt advection averaged over each of the four regions, and the lag at which it occurs (right). Stippling marks areas of significant correlation ($p < 0.01$), and the boxes show the regions of the Ross Sea and the Amundsen/Bellingshausen seas focused on in this section.

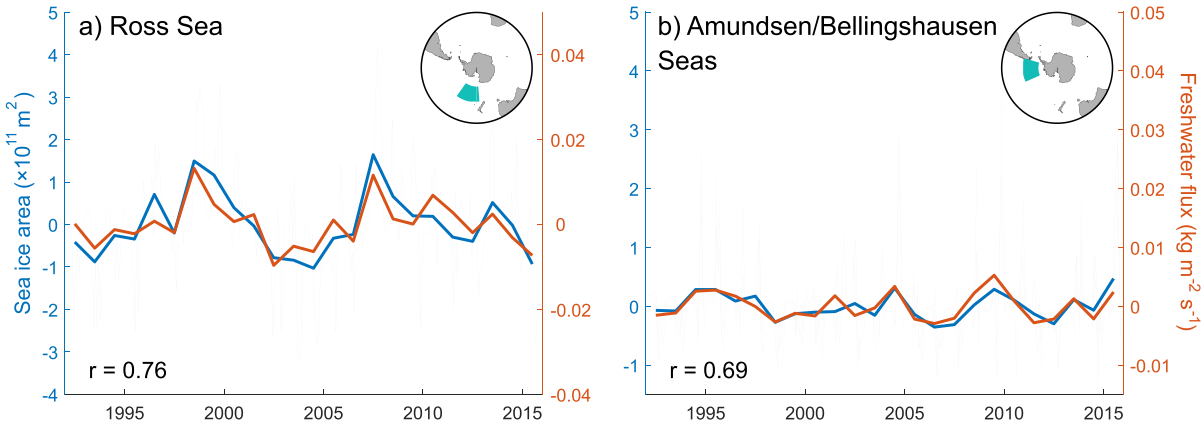

Figure 6. Detrended anomalies in ECCO total sea ice area (m^2, blue) and the surface freshwater flux due to sea ice (kg m^{-2} s^{-1}, red), averaged over the region north of 66°S in (a) the Ross Sea (175°E−145°W) and (b) the northern Amundsen/Bellingshausen seas (74–114°W) The correlation coefficient, *r*, between the two variables is also shown ($p < 0.01$).

to reach the SEPSAMW formation region farthest from the Ross Sea sea ice edge. This advective timescale aligns well with numerical particle release experiments over similar regions (Cerovečki et al., 2019).

Similar significant negative correlation can be seen between ECCO sea ice area and the zonal component of the advection (Figure 7b), suggesting that zonal advection provides the primary direction of transport of freshwater anomalies originating in the Ross Sea entering the SAMW formation regions. Correlation with only zonal advection is slightly weaker in the CPPF box, pointing to the delivery of freshwater anomalies to this region with a significant meridional advection component, as is shown by the significant negative correlation also seen in the meridional component of advection (Figure 7c). This is intuitive, as a proportion of the sea ice area is directly south of the CPPF box. There is no significant correlation with meridional advection in the SEPPF box, due to the relative positions of the sea ice and formation region, and the potential for confounding meridional signals from more closely located Amundsen and Bellingshausen sea ice. Correlation in the CPSAMW formation region is slightly stronger with meridional advection, but with a much longer lag of 25 months. This suggests that freshwater anomalies are transported both north and east from the sea ice edge into the CPSAMW formation region. There is no significant negative correlation with meridional advection in the SEPSAMW formation region, indicating that freshwater anomalies are advected north into the CPSAMW formation region, then east along the ACC into the SEPSAMW formation region. Again, this aligns with particle trajectories in previous studies.

The strength and optimum lag of the correlation suggests that freshwater anomalies enter the CPPF box via northeastward advection. Anomalies are then transported further northeast as well as directly east within the mean ACC flow, reaching the SEPPF and CPSAMW regions around the same time. Anomalies in the CPSAMW region are then advected further east, reaching the SEPSAMW region around 2 years after the initial maximum sea ice extent. Given the maximum sea ice extent typically occurs in September, the strongest freshwater anomalies would be expected to be observed the following December in the CPPF box, around a year later in the SEPPF box and CPSAMW formation region, and around the austral summer 2 years after the maximum sea ice extent in the SEPSAMW formation region. While SAMW subduction occurs in winter, freshwater anomalies reaching the SAMW formation regions during summer could play a role in setting the properties of the mixed layer, prior to the development of the deep winter mixed layers and the formation of SAMW.

3.5. Link Between Amundsen and Bellingshausen Sea Ice and Salt Advection in ECCO

Only total and meridional salt advection in the southeast water mass formation regions is significantly ($p < 0.05$) correlated with sea ice in the Amundsen/Bellingshausen seas (Figure 8), as the sea ice region is directly south of the water mass formation sites. Significant correlation in the SEPPF box occurs at lags of 0–2 months, peaking at two months due to the proximity of the region to the sea ice, and significant correlation in the SEPSAMW formation region occurs at lags of 2–13 months, peaking at 6 months. The correlation is stronger when only the meridional component of advection is considered, suggesting that zonal advective fluxes for this box have sources elsewhere, as described in the previous section. Negative correlation with meridional advection in the SEPPF box

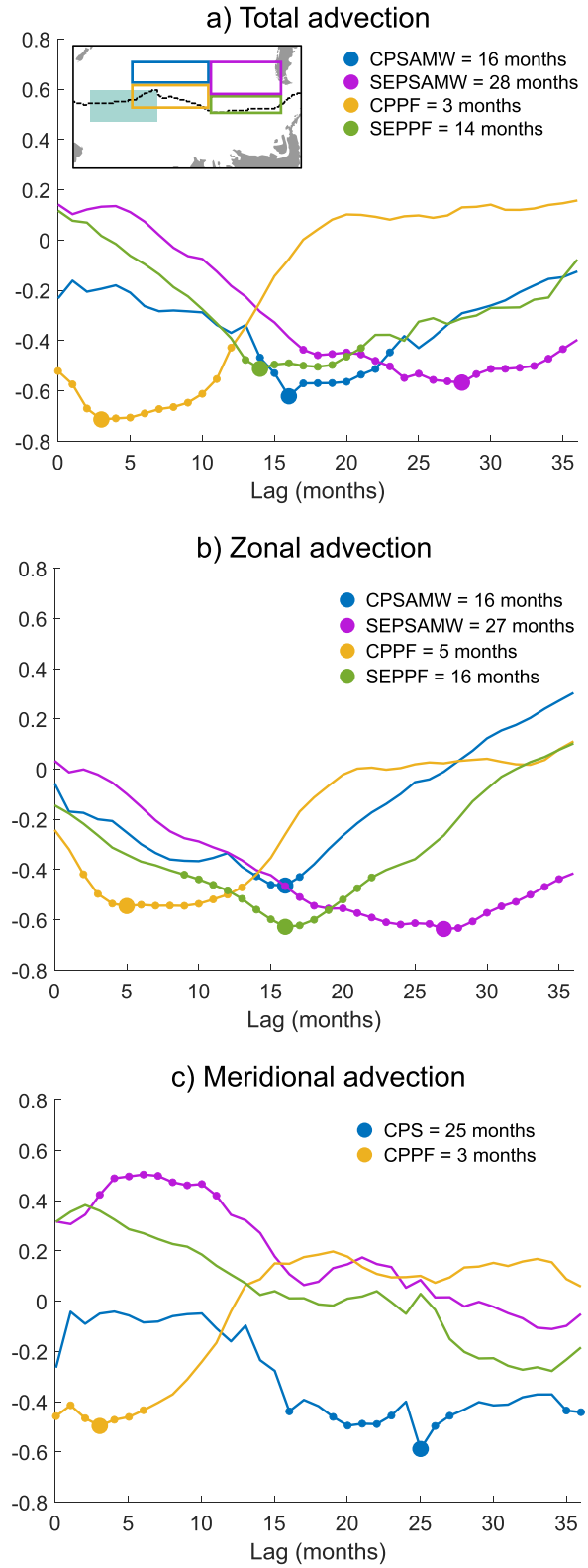

Figure 7. Correlation coefficient between the ECCO salt advection averaged over each water mass formation region, and annual averaged sea ice area in the northern Ross Sea, for lags of 0–36 months. The same is shown for only (b) zonal, and (c) meridional advection. Dots mark 95% significant negative correlation, and the lag for the strongest correlation is noted in the legend. The sea ice region (shaded area) and maximum sea ice extent (dotted line) in relation to the water mass formation regions are shown on the inset map.

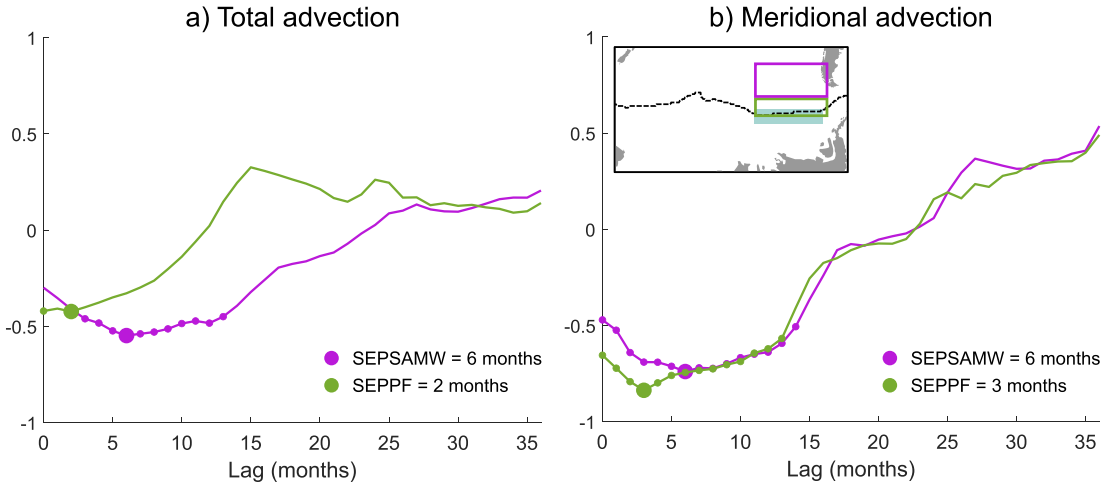

Figure 8. (a) Correlation coefficient between the ECCO salt advection averaged over the southeast water mass formation regions, and annual averaged sea ice area in the northern Amundsen/Bellingshausen seas, for lags of 0–36 months. (b) The same for only meridional advection. Dots mark 95% significant negative correlation, and the lag for the strongest correlation is noted in the legend. The sea ice region (shaded area) and maximum sea ice extent (dotted line) in relation to the water mass formation regions are shown on the inset map.

occurs at lags of 0–13 months, with a maximum correlation of −0.84 at a three month lag. In the SEPSAMW formation region, the correlation is significant at lags of 0–14 months, peaking at 6 months with a correlation coefficient of −0.74.

Maximum sea ice extent typically occurs in September, so based on the strongest correlations with meridional advection, the strongest freshwater anomalies would be expected to reach the SEPPF and SEPSAMW formation regions the following December and March, respectively. While the lag in correlation relates to the winter maximum sea ice area, the deposition of freshwater into the ocean happens shortly after, and the advection speed is therefore faster than the lag in correlation suggests. Initial deepening of the mixed layer, prior to the complete development of deep winter mixed layers and subsequent SAMW subduction, occurs in autumn. Hence an input of anomalous freshwater into the region during the summer and autumn could precondition the surface waters before mixed layer deepening, and influence the properties of the winter mixed layer.

3.6. Causes of the 2016 Mixed Layer Anomalies in B-SOSE

As in observations, the B-SOSE mixed layer is anomalously deep in the CPSAMW formation region during the winter of 2016, reaching approximately 500 m, while the mixed layer in the SEPSAMW formation region fails to deepen to more than 220 m (Figures 9a and 9b). This anomalously shallow winter mixed layer occurs after the strongest summer surface warming of the B-SOSE mixed layer budget, and leads to anomalously low entrainment (Figure 3). The anomalies become apparent in the CPSAMW formation region in June 2016, when MLD is four standard deviations greater than the mean (Figure 10a). The mixed layer then remains at least one standard deviation deeper than the mean until October. Throughout the year, the temperature of the mixed layer is within one standard deviation of the average (Figure 10c), while salinity is consistently higher than the model average (Figure 10e), reaching a maximum of 34.33 psu in September 2016, compared to a mean of 34.30 ± 0.01 psu. The lack of development of the winter mixed layer in the SEPSAMW formation region begins in May, when the mixed layer is two standard deviations shallower than the mean. The difference becomes greater as the winter mixed layer forms, and persists until November. The mixed layer is anomalously fresh and warm during the autumn/winter of 2016 (Figures 10d and 10f). Salinity peaks at 34.06 psu in October, a month later than the average seasonal maximum of 34.11 ± 0.03 psu. Temperature reaches a minimum of 5.35°C in September, compared to an average of 4.89 ± 0.17°C.

Initial low temperature tendency in the CPSAMW formation region is due to lower than average surface heating (Figure 11a) and increased cooling via advection (Figure 11c), while more positive surface fluxes and advection in April drive a positive temperature tendency. Note that the surface flux terms of the mixed layer budgets represent the impact of air-sea fluxes on mixed layer temperature/salinity and are heavily influenced by the MLD. The

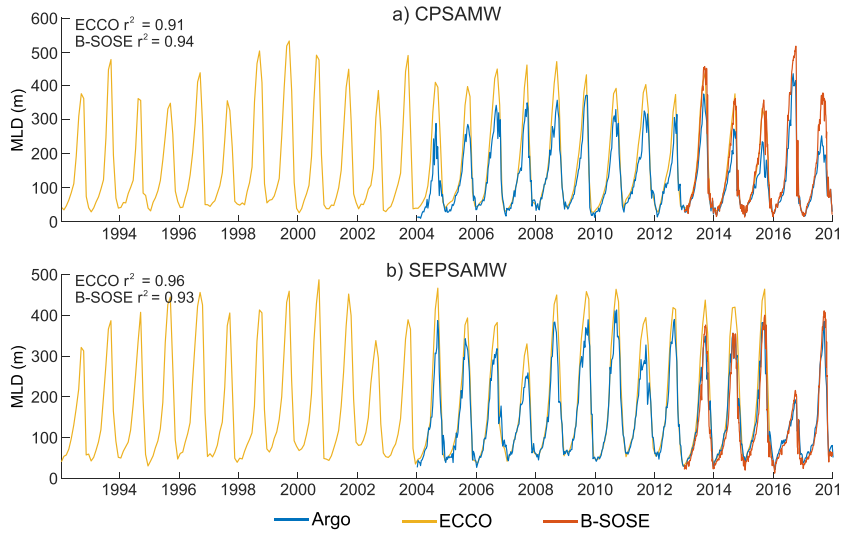

Figure 9. Mixed-layer depth (m) averaged over the (a) CPSAMW and (b) SEPSAMW formation regions for each model, in comparison to Argo observations. The r2 value between each model time series and the corresponding Argo observations is also shown.

model output net heat flux is in fact anomalously low (higher surface heat loss) from May to October 2016, but the effect of this is masked by the anomalously deep mixed layer. Advection during the start of 2016 drives only a small change in salinity (Figure 12c); with a salinity increase of 0.01 psu yr^{-1} during April, compared to an average freshening of -0.18 ± 0.10 psu yr^{-1}. Advection then remains more than one standard deviation above the mean until September. A strong freshwater flux of -0.65 psu yr^{-1} in February 2016, compared to a mean of -0.05 ± 0.17 psu yr^{-1}, is not enough to dramatically alter mixed layer salinity, which remains within one standard deviation of the mean.

Warming and freshening of the mixed layer in the SEPSAMW formation region in January 2016 is mainly due to strong surface fluxes (Figure 11b), driving a warming of 33.54°C yr^{-1} (compared to a mean of 22.94 ± 5.21°C yr^{-1}), and a freshening of -0.60 psu yr^{-1} (compared to a mean of -0.23 ± 0.20 psu yr^{-1}). From February–March, advection drives a maximum cooling of -2.98°C yr^{-1}, compared to an average of -1.84 ± 0.86°C yr^{-1} (Figure 11d), and a maximum freshening of -0.35 psu yr^{-1}, compared to an average of -0.18 ± 0.16 psu yr^{-1}. The advective cooling and freshening is due to meridional advection, while zonal advection drives a lesser warming and salinity increase (see Sanders (2021)). In May, a strong increase in temperature tendency is due to lower surface heat loss and advection. Surface fluxes cause a cooling of -2.10°C yr^{-1}, more than five standard deviations higher than the mean of -7.55 ± 0.80°C yr^{-1}. Previous studies have linked this to a decrease in the number of winter storms (Ogle et al., 2018). While anomalies in the surface flux term of the budget are only present until the following month, anomalies in the model output surface flux term persist from May until August. Simultaneous advection drives a warming of 0.66°C yr^{-1}, compared to a mean cooling of -0.87 ± 0.63°C yr^{-1}. Over winter, advection drives a stronger than average increase in both temperature and salinity, while surface freshwater fluxes lead to anomalous freshening. The shallow winter mixed layer results in the lower entrainment seen in Figure 3, leading to negative feedback due to a lack of colder, higher-salinity water being entrained into the mixed layer. From July onwards, high salt advection brings the average mixed layer salinity of the region back within one standard deviation of the mean.

Surface fluxes drive obvious anomalies in the properties of the SAMW formation region mixed layers. The surface flux terms shown in Figures 11 and 12 are dependent on MLD. If the mixed layer is deep, surface fluxes have a lower impact on the average mixed layer temperature/salinity, as they must act on a larger volume of water. A shallower mixed layer is therefore more susceptible to changes in surface fluxes. In the case of very weak stratification at the base of the mixed layer, small changes in temperature and salinity would drive convection as it is easier for them to overcome the stratification, and so surface fluxes can still impact MLD via convection. In the case of convecting mixed layers, surface fluxes will also have a smaller apparent impact on the mixed layer properties due to compensating entrainment as the mixed layer deepens.

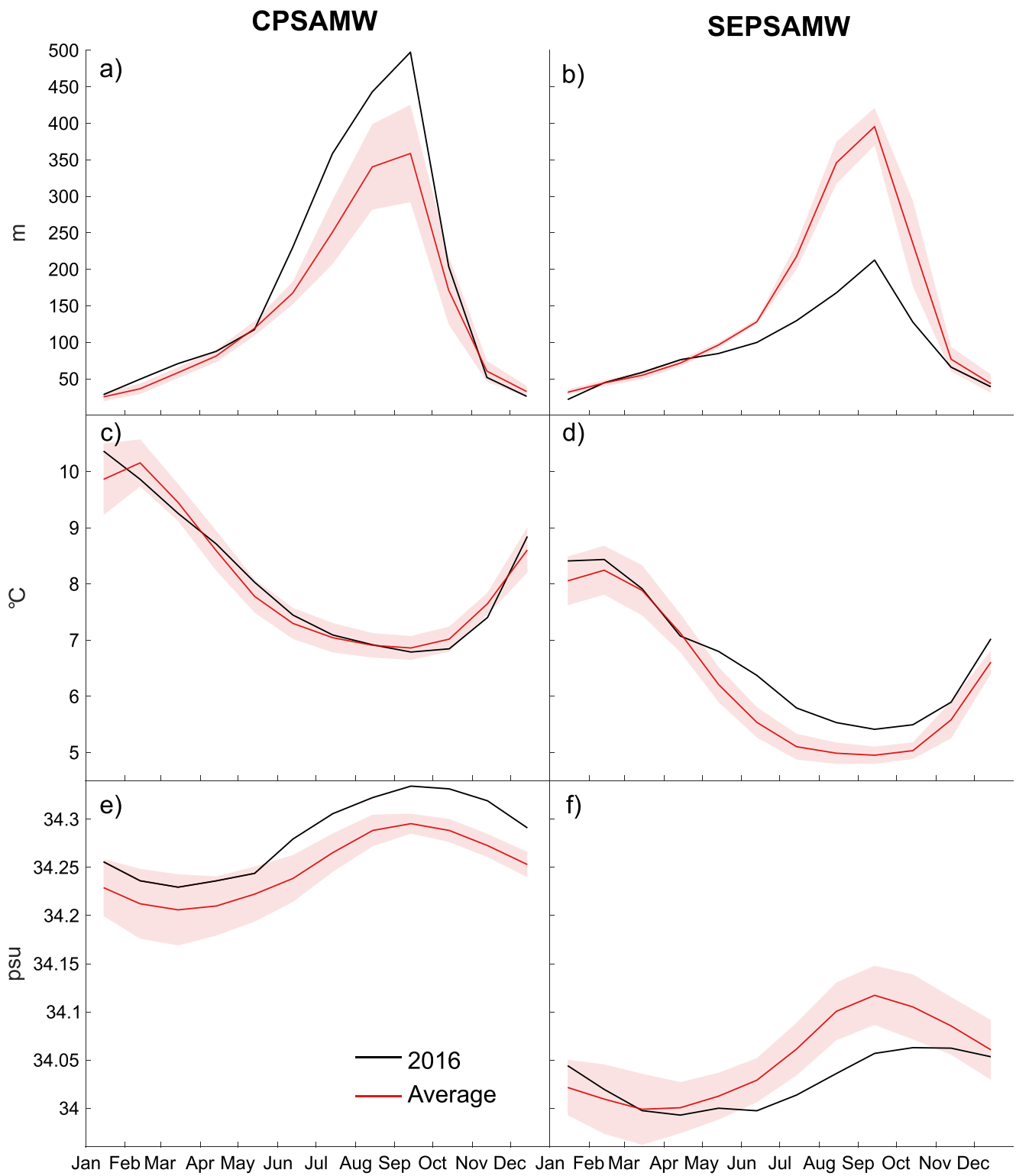

Figure 10. Monthly averaged B-SOSE mixed layer (a), (b) depth (m), (c), (d) temperature (°C), and (e), (f) salinity (psu) in 2016 (black), compared with the average and standard deviation for the remaining time series (red) in the CPSAMW (left) and SEPSAMW (right) formation regions.

The timing of the MLD anomalies in the CPSAMW formation region coincides with both anomalous surface cooling and salt advection. In the SEPSAMW formation region, the anomalously weak surface cooling clearly aligns with the anomalously low rate of deepening of the mixed layer in B-SOSE. For the longer ECCO time series, winter MLD and total heat flux from May to September are significantly correlated, with a correlation

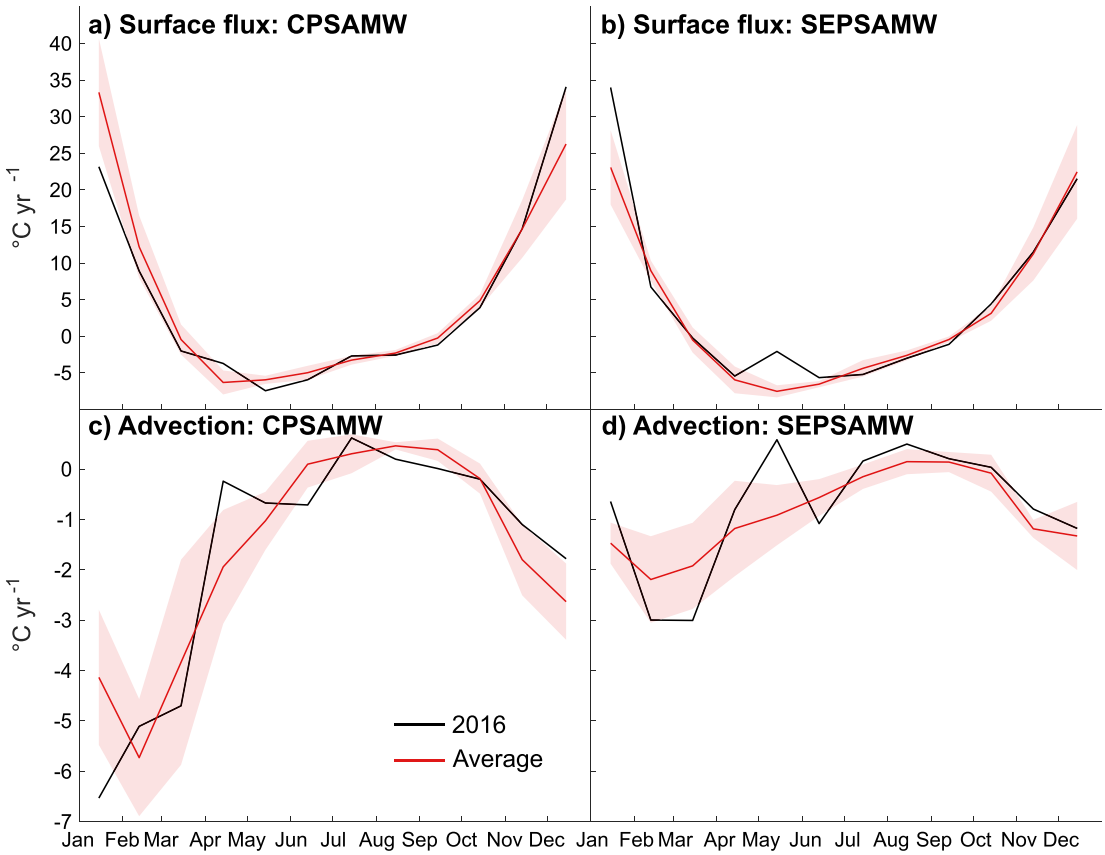

Figure 11. Monthly averaged B-SOSE mixed layer temperature budget surface flux and advection terms (°C yr^{-1}), averaged over the CPSAMW (left) and SEPSAMW (right) formation regions, for 2016 (black), and the mean and standard deviation of the remaining time series (red).

coefficient of −0.71 in the CPSAMW formation region, and −0.52 in the SEPSAMW formation region ($p < 0.01$). However, there are still years when the surface heat flux is high while the mixed layer is deep, suggesting other processes play a role in driving interannual variability in the MLD of the SAMW formation regions. During 2016, salt advection is also anomalous, acting to freshen the SEPSAMW formation region mixed layer and increase salinity in the CPSAMW formation region mixed layer during the lead up to the deepening of the mixed layer.

Advective freshening from January to March 2016 in the SEPSAMW formation region is predominantly due to meridional advection that can be related to sea ice changes directly to the south. As seen in observations (Parkinson, 2019), sea ice extent in the Amundsen and Bellingshausen seas was high during 2015, peaking from August to September. Therefore, assuming the correlations seen in ECCO are a result of sea ice driving variability in freshwater advection, anomalies in the SEPSAMW formation region would be expected around 6 months later, from February to March, that is, when meridional advection drives a cooling and freshening of the mixed layer during 2016, helping to reduce the mixed layer salinity to the low levels observed during the winter of 2016.

Another key feature of the B-SOSE salinity budget is the absence of advective freshening from January to April 2017 in the SEPSAMW formation region (Figure 13b). In every other year, advection drives a freshening of −0.16 to −0.36 psu yr^{-1} during this period, suggesting that the usual salinity gradient between the sea ice edge and the SEPSAMW formation region is greatly reduced in 2017. The mixed layer in the summer of 2017 has the highest salinity of the B-SOSE time series, and the subsequent winter mixed layer is the deepest, reaching 429 m. The anomalous advection is a result of both zonal and meridional advective fluxes, with meridional advection driving a salinity increase in January/February of up to 0.10 psu yr^{1}, and zonal advection driving a maximum salinity increase of 0.14 psu yr^{1} in March. Only one other year (2014) does not show freshening via meridional advection during summer. A dramatic reduction in sea ice occurs in the winter of 2016 in the Amundsen/Bellingshausen seas region, reaching a seasonal maximum in August 2016 that is less than a third of that of the

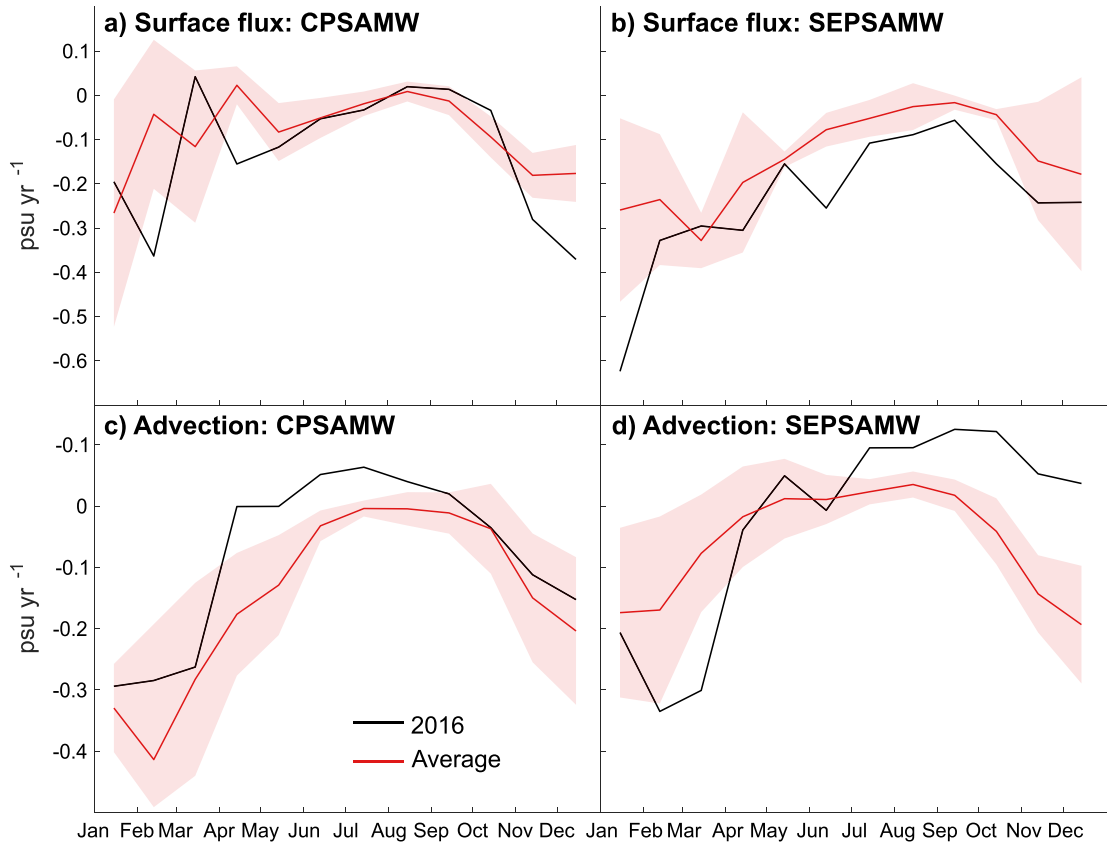

Figure 12. Monthly averaged B-SOSE mixed layer salinity budget surface flux and advection terms (psu yr^{-1}), averaged over the CPSAMW (left) and SEPSAMW (right) formation regions, for 2016 (black), and the mean and standard deviation of the remaining time series (red).

next lowest year (Figure 13a). The lag between the low winter sea ice extent and positive salt advection in the SEPSAMW formation region matches that of the correlation seen in ECCO, suggesting the reduction in sea ice is at least partially responsible.

4. Discussion

4.1. Drivers of Variability in the SAMW Formation Regions

The dominance of surface heat and freshwater fluxes on the mixed layer budgets of the main Pacific SAMW formation regions supports previous observational studies suggesting that it is surface fluxes, and in particular heat fluxes, that drive the majority of seasonal variability in the SAMW formation regions, and drive the deep winter convection associated with the formation of the water mass (Holte et al., 2012; Tamsitt et al., 2020). While previous studies have suggested that lateral induction plays an important role in driving subduction within SAMW formation regions (Hong et al., 2021; Sallée et al., 2010), we find that the horizontal heat and salt gradients do not have strong enough components or divergences aligned with velocity fields for the process to drive significant changes in mixed layer temperature and salinity. In studies such as Sallée et al. (2010), the horizontal gradients in MLD and velocities are from independent data sets, and so may not always be accurately aligned, allowing larger covariances that do not exist in a dynamically consistent single model data set used here.

In addition to the dominance of surface forcing, we find that entrainment and horizontal advection play major roles in driving salinity variability. A strong annual increase via entrainment is intuitive, considering the intense deepening of the mixed layer within the SAMW formation regions during winter. However, it is likely that the magnitude of the process is under-represented in ECCO as the monthly averaged output does not fully capture the higher temporal resolution intensity of the deepening of the winter mixed layer seen in B-SOSE.

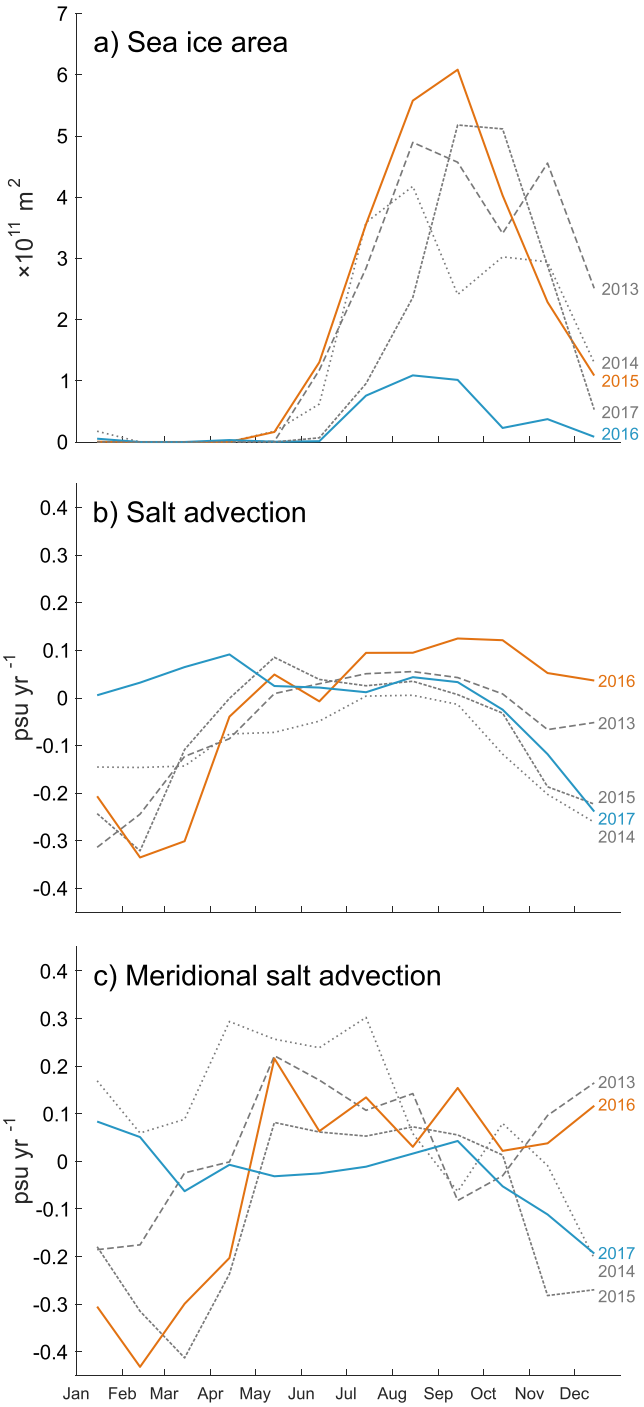

Figure 13. (a) B-SOSE Amundsen and Bellingshausen sea ice area (m^2), (b) salt advection (psu yr^{-1}) and (c) the meridional component of the advection (psu yr^{-1}), averaged over the SEPSAMW formation region. The red lines show the year with highest winter sea ice (2015 in (a)), and subsequent year of initial strong freshwater advection, and the blue lines show the year with lowest winter sea ice (2016 in (a)) and subsequent year of reduced freshwater advection.

4.2. Influence of Sea Ice on Salt Advection

In an effort to find the links between sea ice and SAMW formation site properties hypothesized by previous studies (Cerovečki et al., 2019; Naveira Garabato et al., 2009), we looked at interannual correlations between sea ice and the SAMW properties, and the mixed layer budgets in the intervening ocean pathways that may serve as teleconnectors. The changing significance and corresponding lag of the correlation between salt advection in each water mass formation site and sea ice zones from east to west, supports the theory that the correlation is due to variability in the sea ice area, rather than coincidental covariance between the two terms driven by, for example, variability in the strength of winds over both regions.

The link between Ross Sea sea ice cover and salt advection in the SAMW formation regions supports the findings of a particle release experiment conducted by Cerovečki et al. (2019) using SOSE. This experiment showed that particles from the Ross Sea sea ice edge from 150°E−120°W can take up to two years to reach the SEPSAMW formation site. This area contains the region of sea ice for which we find significant correlation, but also extends further east and west. While we find further correlation between salt advection and sea ice in the Amundsen/Bellingshausen seas, the particle release experiment suggested that freshwater anomalies originating east of 120°W are advected east by the ACC before they reach the SEPSAMW formation region. However, this only considered particles that pass north of the SAF within the longitude range 150°E−120°W. Sources further to the east would likely be observed if all particles that reached the defined SAMW formation boxes were included. The boxes used here, in particular the Polar Front boxes, extend further south of the SAF, allowing freshwater from source regions further east to be considered.

An observed record maximum sea ice extent in the Amundsen/Bellingshausen seas during the winter of 2015 (Parkinson, 2019) is also seen in B-SOSE, and is followed by anomalous advective freshening of the SEPPF box and SEPSAMW formation region up to 6 months later. While the time series of the model is too short to determine correlations in interannual variability, this event supports the correlations found in ECCO, with the timings of freshwater advection into the SEPSAMW formation region matching the lags of the correlations. Following the large reduction in Antarctic sea ice in 2016 (Schlosser et al., 2018; Turner et al., 2017), a clear reduction in freshwater advection in the SEPSAMW formation region is seen in B-SOSE in the summer/autumn of 2017. Following this regime change in Antarctic sea ice, more positive salt advection could be expected into the SAMW formation regions, due to the decrease in melt at the sea ice edge, incorporating less freshwater into the upper cell of the Southern Ocean overturning circulation.

4.3. The Impact of Salt Advection on SAMW

While surface buoyancy fluxes are the dominant drivers of deep convection in the region (Holte et al., 2012; Ogle et al., 2018; Tamsitt et al., 2020), advection shows strong interannual variability. The lag of the significant correlation between sea ice and salt advection suggests that freshwater anomalies due to sea ice melt in both the Ross Sea and the Amundsen/Bellingshausen seas reach the SAMW formation during austral summer and autumn, and so have the potential to stabilize the water column and reduce the subsequent winter convection and formation of SAMW. In 2016, the extreme difference in MLD between the two SAMW formation regions can be attributed to anomalies in surface heat fluxes; however, concurrent anomalies in the

salinity of the SEPSAMW formation region are primarily driven by salt advection. The advection in anomalies the SEPSAMW formation region are linked with high sea ice in the Amundsen/Bellingshausen seas the previous winter. The following year, when salt advection did not drive a freshening due to the extreme low sea ice concentration in the Amundsen/Bellingshausen seas, the region experienced the highest salinity of the time series. Changes in the SAMW formation regions prior to wintertime subduction may act to precondition the mixed layer, allowing anomalous surface fluxes to have a larger impact on the intensity of the convection. Changes in convection are particularly important because the depth of the winter mixed layer drives variability in the thickness of the SAMW formed, and ultimately the volume of the water mass (Meijers et al., 2019) and the heat and carbon uptake (Gao et al., 2018; Jing & Luo, 2021; Roemmich et al., 2015).

4.4. Caveats of the Mixed Layer Budgets

We approximated the mixed layer temperature and salinity budgets offline using the ECCO monthly averaged output, following the example of many previous studies (Close & Goosse, 2013; Dong et al., 2007, 2009; Frankignoul, 1985; Peter et al., 2006; Ren et al., 2011). This allows us to assign changes in mixed layer temperature and salinity to known physical processes. The method incorporates the dynamic nature of the mixed layer, and so gives an insight into the impact of the evolution of the mixed layer that is not available in a closed-budget representation, where the budget is calculated in each model cell individually. Considering the dynamic nature of the mixed layer is essential within the SAMW formation regions, where the depth of the winter mixed layer can reach up to 500 m (McCartney, 1977) and seasonal deepening plays an important role in setting the properties of the mixed layer itself. Another benefit of this method is that it can be applied universally to any data set, including observations.

The obvious disadvantage of this method is that the budgets do not fully close. Reasons for this include the lower temporal resolution data that the budgets are computed on in comparison to when closed budgets are computed online, and the error introduced as a result of the constant values chosen for diffusivity, and the definition of entrainment velocity. However, the majority of the variability in mixed layer temperature and salinity was captured for each budget, and the advection terms, focused on primarily in this work, are the same for online-computed, closed budgets.

While there are many advantages to using a state estimate to investigate ocean variability, particularly when computing budgets, there are also caveats that should be considered. There will be some differences between the output of the two models due to the optimization process of the state estimates. ECCO also has a relatively coarse spatial resolution, however the model mixing parameters are optimized during the state estimation to represent unresolved processes (Forget, Ferreira, & Liang, 2015). While B-SOSE has a higher spatio-temporal resolution, it covers a much shorter period, making it more difficult to investigate interannual variability. While ECCO has lower spatio-temporal resolution, mismatch from the observations in MLD is only slightly higher than in B-SOSE (Figure 9), with an r^2 value of at least 0.91 between MLD and observations in each SAMW formation region. Interannual variability in MLD matches particularly well, giving further confidence to the results. Previous work has suggested that when only the spatio-temporal resolution of a model is changed, there is no qualitative change to the results of mixed layer budgets within this region (Sanders, 2021). Despite the drawbacks of the state estimates, we find that the same processes are responsible for the majority of temperature and salinity variability in the SAMW formation regions in both models, giving us further confidence in the budget results. Sea ice area in ECCO is also similar to observations for both the northern Ross Sea and the Amundsen/Bellingshausen Seas, with an r^2 value of at least 0.7 in each model (Figure S1, https://nsidc.org/data/g02202/versions/4), and the same interannual variability can be seen clearly in each data set.

5. Conclusions

We used the ECCO and B-SOSE ocean state estimates to analyze drivers of variability in the mixed layers of the Pacific SAMW formation regions, and investigate the connection with Antarctic sea ice change. Anomalies from the seasonal cycle in salt advection were found to be strongly correlated with sea ice area in the Ross Sea at lags of up to 2 years, while anomalies in the SEPSAMW formation region were also found to correlate with sea ice in the Amundsen/Bellingshausen seas at lags of up to 6 months. Strong anomalies in the winter MLD during 2016 were associated with anomalously low surface heat loss in the SEPSAMW formation region. These anomalies were

preceded by strong advective freshening in the lead up to convection, linked to high sea ice in the Amundsen/Bellingshausen seas the previous winter, and suggesting the possibility of preconditioning of the winter mixed layer. Advection was shown to be an important driver of salinity change in the SAMW formation region on interannual timescales, while surface fluxes and entrainment were also found to be important on seasonal timescales. Lateral induction and horizontal diffusion played a negligible role in driving variability in either region. Repeating the analysis on data from the most recent record low sea ice years (austral summers of 2021/22 and 2022/23) would be useful to further understand the impact of sea ice on SAMW properties, and to see if there has indeed been a reduction of freshwater advected into the SAMW formation regions, associated with the ongoing sea ice changes. With declining sea ice in future due to climate change, we can expect more years similar to 2017, where the seasonal freshening of SAMW due to sea ice does not occur. If this seasonal advection is indeed preconditioning the mixed layer prior to SAMW formation, reduced freshwater advection could lead to deeper winter mixed layers and stronger subduction.

Data Availability Statement

All data used in this work may be freely obtained from the following sources. The ECCO version 4 release 3 output is accessible from the ECCO Data Portal (https://ecco.jpl.nasa.gov/drive/files/Version4/Release3). The B-SOSE iteration 122 output is evolved from Verdy and Mazloff (2017) and can be found at http://sose.ucsd.edu/BSOSE6_iter122_solution.html. The sea ice data used to validate the models in Figure S1 can be found at https://nsidc.org/data/g02202/versions/4. Argo data were collected and made freely available by the International Argo Program and the national programs that contribute to it (http://www.argo.ucsd.edu, http://argo.jcommops.org). The Argo Program is part of the Global Ocean Observing System. The Argo gridded product used to validate the models in Figures 1 and 9 and Figure S2 was produced by King et al. (2021), https://doi.org/10.5285/961f3c2d-04ca-1911-e053-6c86abc0150b.

Acknowledgments
The authors thank Ivana Cerovecki and Matt Mazloff for their advice computing mixed-layer budgets in the models. This work was supported by the Natural Environmental Research Council [Grant NE/R009783/1].

References

Abernathey, R. P., Cerovecki, I., Holland, P. R., Newsom, E., Mazloff, M., & Talley, L. D. (2016). Water-mass transformation by sea ice in the upper branch of the Southern Ocean overturning. *Nature Geoscience*, *9*(8), 596–601. https://doi.org/10.1038/ngeo2749

Beadling, R. L., Russell, J., Stouffer, R., Mazloff, M., Talley, L., Goodman, P., et al. (2020). Representation of Southern Ocean properties across coupled model intercomparison project generations: CMIP3 to CMIP6. *Journal of Climate*, *33*(15), 6555–6581. https://doi.org/10.1175/JCLI-D-19-0970.1

Boehme, L., Meredith, M. P., Thorpe, S. E., Biuw, M., & Fedak, M. (2008). Antarctic Circumpolar Current frontal system in the South Atlantic: Monitoring using merged Argo and animal-borne sensor data. *Journal of Geophysical Research*, *113*(C9), C09012. https://doi.org/10.1029/2007JC004647

Boland, E. J., Jones, D. C., Meijers, A. J., Forget, G., & Josey, S. A. (2021). Local and remote influences on the heat content of Southern Ocean mode water formation regions. *Journal of Geophysical Research: Oceans*, *126*(4), e2020JC016585. https://doi.org/10.1029/2020JC016585

Cerovečki, I., & Meijers, A. J. (2021). Strong quasi-stationary wintertime atmospheric surface pressure anomalies drive a dipole pattern in the Subantarctic ModeWater formation. *Journal of Climate*, 1–44. https://doi.org/10.1175/JCLI-D-20-0593.1

Cerovečki, I., Meijers, A. J. S., Mazloff, M. R., Gille, S. T., Tamsitt, V. M., & Holland, P. R. (2019). The effects of enhanced sea ice export from the Ross Sea on recent cooling and freshening of the Southeast Pacific. *Journal of Climate*, *32*(7), 2013–2035. https://doi.org/10.1175/JCLI-D-18-0205.1

Close, S. E., & Goosse, H. (2013). Entrainment-driven modulation of Southern Ocean mixed layer properties and sea ice variability in CMIP5 models. *Journal of Geophysical Research: Oceans*, *118*(6), 2811–2827. https://doi.org/10.1002/jgrc.20226

Comiso, J. C., & Nishio, F. (2008). Trends in the sea ice cover using enhanced and compatible AMSR-E, SSM/I, and SMMR data. *Journal of Geophysical Research*, *113*(C2), C02S07. https://doi.org/10.1029/2007JC004257

de Boyer Montégut, C., Madec, G., Fischer, A. S., Lazar, A., & Iudicone, D. (2004). Mixed layer depth over the global ocean: An examination of profile data and a profile-based climatology. *Journal of Geophysical Research*, *109*(C12), C12003. https://doi.org/10.1029/2004JC002378

Dong, S., Garzoli, S. L., & Baringer, M. (2009). An assessment of the seasonal mixed layer salinity budget in the Southern Ocean. *Journal of Geophysical Research*, *114*(C12), C12001. https://doi.org/10.1029/2008JC005258

Dong, S., Gille, S. T., & Sprintall, J. (2007). An assessment of the Southern Ocean mixed layer heat budget. *Journal of Climate*, *20*(17), 4425–4442. https://doi.org/10.1175/JCLI4259.1

Downes, S. M., Langlais, C., Brook, J. P., & Spence, P. (2017). Regional impacts of the westerly winds on Southern Ocean mode and intermediate water subduction. *Journal of Physical Oceanography*, *47*(10), 2521–2530. https://doi.org/10.1175/JPO-D-17-0106.1

ECCO Consortium. (2017a). A twenty-year dynamical oceanic climatology: 1994–2013. Part 1: Active scalar fields: Temperature, salinity, dynamic topography, mixed-layer depth, bottom pressure (Tech. Rep.). Retrieved from http://hdl.handle.net/1721.1/107613

ECCO Consortium. (2017b). A twenty-year dynamical oceanic climatology: 1994–2013. Part 2: Velocities, property transports, meteorological variables, mixing coefficients (Tech. Rep.). Retrieved from http://hdl.handle.net/1721.1/109847

Forget, G., Campin, J. M., Heimbach, P., Hill, C. N., Ponte, R. M., & Wunsch, C. (2015). ECCO version 4: An integrated framework for non-linear inverse modeling and global ocean state estimation. *Geoscientific Model Development*, *8*(10), 3071–3104. https://doi.org/10.5194/gmd-8-3071-2015

Forget, G., Ferreira, D., & Liang, X. (2015). On the observability of turbulent transport rates by Argo: Supporting evidence from an inversion experiment. *Ocean Science*, *11*(5), 839–853. https://doi.org/10.5194/os-11-839-2015

Frankignoul, C. (1985). Sea surface temperature anomalies, planetary waves, and air-sea feedback in the middle latitudes. *Reviews of Geophysics*, *23*(4), 357–390. https://doi.org/10.1029/RG023i004p00357

Fukumori, I., Wang, O., Fenty, I., Forget, G., Heimbach, P., & Ponte, R. M. (2017). ECCO version 4 release 3 [Dataset] (Tech. Rep.). Retrieved from https://dspace.mit.edu/handle/1721.1/110380

Gao, L., Rintoul, S. R., & Yu, W. (2018). Recent wind-driven change in Subantarctic Mode Water and its impact on ocean heat storage. *Nature Climate Change*, *8*(1), 58–63. https://doi.org/10.1038/s41558-017-0022-8

Haumann, F. A., Gruber, N., Münnich, M., Frenger, I., & Kern, S. (2016). Sea-ice transport driving Southern Ocean salinity and its recent trends. *Nature*, *537*(7618), 89–92. https://doi.org/10.1038/nature19101

Holland, P. R., & Kwok, R. (2012). Wind-driven trends in Antarctic sea-ice drift. *Nature Geoscience*, *5*(12), 872–875. https://doi.org/10.1038/ngeo1627

Holte, J. W., Talley, L. D., Chereskin, T. K., & Sloyan, B. M. (2012). The role of air-sea fluxes in Subantarctic Mode Water formation. *Journal of Geophysical Research*, *117*(C3), C03040. https://doi.org/10.1029/2011JC007798

Hong, Y., Du, Y., Xia, X., Xu, L., Zhang, Y., & Xie, S.-P. (2021). Subantarctic mode water and its long-term change in CMIP6 models. *Journal of Climate*, *34*(23), 9385–9400. https://doi.org/10.1175/JCLI-D-21-0133.1

Huang, R. X. (1990). On the three-dimensional structure of the wind-driven circulation in the North Atlantic. *Dynamics of Atmospheres and Oceans*, *15*(1–2), 117–159. https://doi.org/10.1016/0377-0265(90)90006-H

Ito, T., Woloszyn, M., & Mazloff, M. (2010). Anthropogenic carbon dioxide transport in the Southern Ocean driven by Ekman flow. *Nature*, *463*(7277), 80–83. https://doi.org/10.1038/nature08687

Jersild, A., & Ito, T. (2020). Physical and biological controls of the drake passage pCO_2 variability. *Global Biogeochemical Cycles*, *34*(9), e2020GB006644. https://doi.org/10.1029/2020gb006644

Jing, W., & Luo, Y. (2021). Volume budget of subantarctic mode water in the Southern Ocean from an ocean general circulation model. *Journal of Geophysical Research: Oceans*, *126*(10), e2020JC017040. https://doi.org/10.1029/2020JC017040

King, B. A., McDonagh, E., & Desbruyeres, D. (2021). Objectively mapped Argo profiling float data from the Global Ocean [Dataset]. British Oceanographic Data Centre, National Oceanography Centre, NERC, 2004–2020. https://doi.org/10.5285/961f3c2d-04ca-1911-e053-6c86abc0150b

McCartney, M. S. (1977). Subantarctic mode water. In *A Voyage of Discovery: George Deacon 70th Anniversary Volume*, (pp. 103–119). Pergamon Press.

Meier, W. N., Fetterer, F., Windnagel, A. K., & Stewart, J. S. (2021). NOAA/NSIDC climate data record of passive microwave sea ice concentration version 4 [Dataset]. National Snow and Ice Data Center. https://doi.org/10.7265/efmz-2t65

Meijers, A. J. S., Cerovečki, I., King, B. A., & Tamsitt, V. (2019). A see-saw in Pacific Subantarctic Mode Water formation driven by atmospheric modes. *Geophysical Research Letters*, *46*(22), 13152–13160. https://doi.org/10.1029/2019GL085280

Naveira Garabato, A. C., Jullion, L., Stevens, D. P., Heywood, K. J., & King, B. A. (2009). Variability of subantarctic mode water and Antarctic intermediate water in the drake passage during the late-twentieth and early-twenty-first centuries. *Journal of Climate*, *22*(13), 3661–3688. https://doi.org/10.1175/2009JCLI2621.1

Ogle, S. E., Tamsitt, V., Josey, S. A., Gille, S. T., Cerovečki, I., Talley, L. D., & Weller, R. A. (2018). Episodic Southern Ocean heat loss and its mixed layer impacts revealed by the farthest south multiyear surface flux mooring. *Geophysical Research Letters*, *45*(10), 5002–5010. https://doi.org/10.1029/2017GL076909

Parkinson, C. L. (2019). A 40-y record reveals gradual Antarctic sea ice increases followed by decreases at rates far exceeding the rates seen in the Arctic. *Proceedings of the National Academy of Sciences*, *116*(29), 14414–14423. https://doi.org/10.1073/pnas.1906556116

Parkinson, C. L., & Cavalieri, D. J. (2012). Antarctic sea ice variability and trends, 1979–2010. *The Cryosphere*, *6*(4), 871–880. https://doi.org/10.5194/tc-6-871-2012

Peter, A.-C., Le Hénaff, M., Du Penhoat, Y., Menkes, C. E., Marin, F., Vialard, J., et al. (2006). A model study of the seasonal mixed layer heat budget in the equatorial Atlantic. *Journal of Geophysical Research*, *111*(C6), C06014. https://doi.org/10.1029/2005JC003157

Qu, T., Gao, S., & Fine, R. A. (2020). Variability of the sub-Antarctic mode water subduction rate during the Argo period. *Geophysical Research Letters*, *47*(13), e2020GL088248. https://doi.org/10.1029/2020GL088248

Ren, L., Speer, K., & Chassignet, E. P. (2011). The mixed layer salinity budget and sea ice in the Southern Ocean. *Journal of Geophysical Research*, *116*(C8), C08031. https://doi.org/10.1029/2010JC006634

Roemmich, D., Church, J., Gilson, J., Monselesan, D., Sutton, P., & Wijffels, S. (2015). Unabated planetary warming and its ocean structure since 2006. *Nature Climate Change*, *5*(3), 240–245. https://doi.org/10.1038/nclimate2513

Russell, J. L., Kamenkovich, I., Bitz, C., Ferrari, R., Gille, S. T., Goodman, P. J., et al. (2018). Metrics for the evaluation of the Southern Ocean in coupled climate models and Earth system models. *Journal of Geophysical Research: Oceans*, *123*(5), 3120–3143. https://doi.org/10.1002/2017JC013461

Sabine, C. L., Feely, R. A., Gruber, N., Key, R. M., Lee, K., Bullister, J. L., et al. (2004). The oceanic sink for anthropogenic CO_2. *Science*, *305*(5682), 367–371. https://doi.org/10.1126/science.1097403

Sallée, J.-B., Morrow, R., & Speer, K. (2008). Eddy heat diffusion and subantarctic mode Water formation. *Geophysical Research Letters*, *35*(5), L05607. https://doi.org/10.1029/2007gl032827

Sallée, J.-B., Speer, K., Rintoul, S., & Wijffels, S. (2010). Southern Ocean thermocline ventilation. *Journal of Physical Oceanography*, *40*(3), 509–529. https://doi.org/10.1175/2009jpo4291.1

Sanders, R. N. (2021). *Drivers of variability in Southern Ocean water mass formation regions (Unpublished doctoral dissertation)*. University of Southampton.

Sanders, R. N., Jones, D. C., Josey, S. A., Sinha, B., & Forget, G. (2022). Causes of the 2015 North Atlantic cold anomaly in a global state estimate. *Ocean Science*, *18*(4), 953–978. https://doi.org/10.5194/os-18-953-2022

Schlosser, E., Haumann, F. A., & Raphael, M. N. (2018). Atmospheric influences on the anomalous 2016 Antarctic sea ice decay. *The Cryosphere*, *12*(3), 1103–1119. https://doi.org/10.5194/tc-12-1103-2018

Su, Z. (2017). Preconditioning of Antarctic maximum sea ice extent by upper ocean stratification on a seasonal timescale. *Geophysical Research Letters*, *44*(12), 6307–6315. https://doi.org/10.1002/2017GL073236

Tamsitt, V., Cerovečki, I., Josey, S. A., Gille, S. T., & Schulz, E. (2020). Mooring observations of air–sea heat fluxes in two Subantarctic Mode Water formation regions. *Journal of Climate*, *33*(7), 2757–2777. https://doi.org/10.1175/JCLI-D-19-0653.1

Thomas, S. D., Jones, D. C., Faul, A., Mackie, E., & Pauthenet, E. (2021). Defining Southern Ocean fronts using unsupervised classification. *Ocean Science*, *17*(6), 1545–1562. https://doi.org/10.5194/os-17-1545-2021

Turner, J., Phillips, T., Marshall, G. J., Hosking, J. S., Pope, J. O., Bracegirdle, T. J., & Deb, P. (2017). Unprecedented springtime retreat of Antarctic sea ice in 2016. *Geophysical Research Letters*, *44*(13), 6868–6875. https://doi.org/10.1002/2017GL073656

Verdy, A., & Mazloff, M. R. (2017). A data assimilating model for estimating Southern Ocean biogeochemistry. *Journal of Geophysical Research: Oceans*, *122*(9), 6968–6988. https://doi.org/10.1002/2016JC012650

Wang, R., Nan, F., Yu, F., & Wang, B. (2022). Subantarctic mode water variations in the three southern hemisphere ocean basins during 2004–2019. *Journal of Geophysical Research: Oceans*, *127*(7), e2021JC017906. https://doi.org/10.1029/2021JC017906